Design of a Bioinspired Robotic Hand: Magnetic Synapse Sensor Integration for a Robust Remote Tactile Sensing

Sang-Hun Kim, *Student Member, IEEE*, Sunjong Oh, Kyu Bum Kim, Youngdo Jung, Hyuneui Lim, and Kyu-Jin Cho, *Member, IEEE*

***Abstract*—Integrating tactile sensors into robotic applications is still a challenge because of sensor interconnection and various form factors. Newly developed magnetic synapse sensors have high sensitivity and remote sensing capability, but integration with a robotic finger is an issue because of the air-transmitting tubes that need to be connected from the sensor to the remotely located base unit. This study proposes an integrated design of a multijoint robotic finger with magnetic synapse sensors inspired by the human's joint structure and synapse system. The joint unit inspired by human's finger joints for the usage of the magnetic synapse sensors can easily has hollow channels and insert air-transmitting tubes through a rotating joint compared to the traditional pin joint. The rolling contact joint also minimizes the length variation of the tube when the joint rotates because the center of rotation changes. Modularized sensor units capable of changing the sensor sensitivity and sensing range have been developed and applied to the remote tactile sensing system. A three-finger gripper with three joints per finger with an integrated three-tactile sensor array was prototyped to explore the feasibility of the units. The sensor sensitivity was 0.016 mV/kPa and the sensing range was 350 kPa. The robotic fingers integrated with a high-sensitivity sensor array can grasp objects with various shapes and compliance (i.e., artificial flowers, paper cups, and wine glasses) without damaging the objects using tactile feedback.**

***Index Terms*—Biologically-inspired robots, force and tactile sensing, grasping, grippers and other end-effectors.**

I. Introduction

TACTILE sensing is a key tool for the perception of our environment and an essential tool for a human's direct interaction with objects. Through contact, humans obtain vital information on their surroundings: pressure, vibration, temperature, texture, and softness. The popularity of this field has resulted in the development of a variety of tactile sensors inspired by human touch for robotic grasping and manipulation [1]–[4].

Most research has focused on improving the performance of sensor components by adopting features for attaching flexible electrodes using nanopatterned elastomeric substrate, liquid metals, silver nanowires, and ultrathin substrate [5]–[8] or using stretchable interconnections [9]. Research on wireless sensing elements used in tandem to create a 'robotic skin' has also been published [10], [11]. Despite the amount of research into tactile sensing, the integration of this technology into robotic applications still remains a challenge. Previous literature could provide some clues, including a lack of robustness caused by the unpredictability and unstructured nature of the environment that humans are constantly interacting with [12], [13]. A vulnerable wire interconnection is one of the major reasons that a tactile sensing system's robustness degrades. For sensors attached to multi-joint robots with large workspaces, integrating the sensors is arduous because the wiring must pass through the joints and withstand the active movements of the robot.

Numerous tactile sensors are developed on a variety of principles; hence, each sensor has a characterized form factor. Accordingly, the integration requirements will vary depending on the form factor of the tactile sensor and its robotic applications. Previous studies presented various robotic hands or prostheses with tactile feedback that satisfied the integration requirements, evaluated novel tactile sensors [14], [15], or verified working algorithms using commercialized sensors [16]–[21].

One of the sensors posing an integration challenge is the magnetic synapse sensor. A previous work associated with this research produced a remote flexible tactile sensing system with a magnetic synapse inspired by the human's synaptic transmitter [22]. The advantage of this sensor is that the remote touch tip is physically separated from the magnetic sensor such that electrical wiring interconnection issues are avoided. Moreover, no electrical components are used in the end-effector, thereby creating a dynamically manufacturable and usable product and resulting in a water-safe or extreme-environment applicable product with minimal packaging of sensor elements.

Similar to other sensors, sensor interconnection is a challenging issue for remote tactile sensor integration onto the actuating system. Instead of having electric components and wirings on the fingertip, the magnetic synapse system requires air tubes for transmitting air pressure variations. The tube has a higher

Manuscript received February 24, 2018; accepted June 10, 2018. Date of publication July 9, 2018; date of current version August 2, 2018. This letter was recommended for publication by Associate Editor S. Briot and Editor P. Rocco upon evaluation of the reviewers' comments. This work was supported by the convergence technology development program for the bionic arm through the National Research Foundation of Korea funded by the Ministry of Science and ICT (2015M3C1B2052817 and 2014M3C1B2048177). *(Corresponding authors: Hyuneui Lim; Kyu-Jin Cho.)*

S.-H. Kim, K. B. Kim, and K.-J. Cho are with the Biorobotics Laboratory, Department of Mechanical and Aerospace Engineering, Institute of Advanced Machines and Design, Seoul National University, Seoul 151-744, South Korea (e-mail: pine6710@snu.ac.kr; kbum34@snu.ac.kr; kjcho@snu.ac.kr).

S. Oh, Y. Jung, and H. Lim are with the Department of Nature-Inspired Nanoconvergence Systems, Korea Institute of Machinery and Materials, Daejeon 34103, South Korea (e-mail: ssun@kimm.re.kr; yjung@kimm.re.kr; helim@kimm.re.kr).

This letter has supplemental downloadable multimedia material available at http://ieeexplore.ieee.org, provided by the authors. The Supplementary Materials contain a video of the design of a bioinspired robotic hand with magnetic synapse sensors for a robust remote touch sensing. This material is 43.5 MB in size.

Digital Object Identifier 10.1109/LRA.2018.2853715

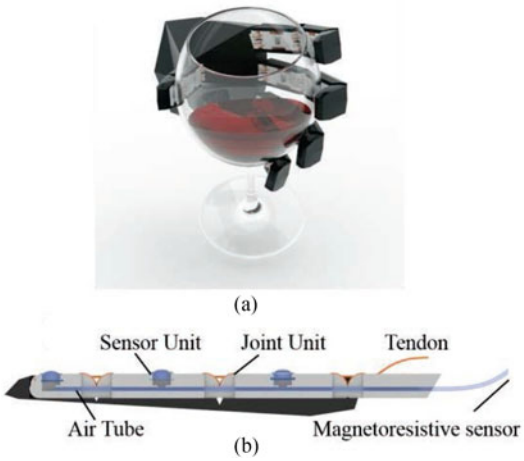

Fig. 1. Illustration of the remote touch tips embedded robotic hand for tactile sensing: (a) a bioinspired robotic hand with grasping a wine glass and (b) cross-sectional view of the robotic finger inspired by human tactile sensing with an air tube that transmits the tactile input.

bending stiffness compared to the signal wires. Therefore, the insertion position of the tubes should be determined to minimize the longitudinal movement of the air tube even if the multiple joints rotate.

This study proposes multi-joint robotic fingers capable of embedding sensors with an air tube with remote touch tips for tactile sensing (Fig. 1(a)). In ensuring that the air tubes are less susceptible to external disturbances, a rolling contact-type joint unit inspired by the human joint structure [23], [24] are used that the tube can pass through its structure (Fig. 1(b)).

Modularized sensor and joint units were developed for ease-of-attachment and detachment to accommodate the tactile sensing replacement and maintenance and address the easy integration of the remote touch tips. The sensitivity and the measuring range of the sensor units can be changed by assembling the sensor and joint units. An underactuated tendon-driven robotic gripper with three tactile sensors located on each distal phalanx was designed. Evaluation experiments were conducted to measure the pressure by grasping cylinders, flowers, paper cups, and wine glasses to grasp the objects without damaging the objects.

II. Design for Sensor Integration

The protruding air-transmitting tube was indispensable because of the characteristics of the remote tactile system using magnetoresistive sensors. The applied modularized rolling contact joints units were capable of embedding the tube to protect sensor interconnection breakaway and distortion from the external disturbance.

A. Magnetoresistive Sensor

Magnetoresistive (MR) sensors are expected to be useful in industrial applications because of their high sensitivity across a broad and dynamic range, having no mechanical hysteresis, and having high physical robustness [1], [25].

The tactile sensor system using MR sensors consisted of a remote touch tip with a soft elastomer membrane for compliant grasping and magnetic synapse physically separated similar to human tactile sensing. In humans, the mechanoreceptors in a fingertip recognize external tactile stimuli and convert them into electrical signals transmitted through the nervous system. Similarly, the remote touch tip transduces an external tactile stimulation caused by the contact of the elastomer membrane with an object by variation of the air pressure, then transmitted to the magnetic synapse through the air tube. The magnetic synapse consisted of a thin elastomeric membrane with a permanent magnet embedded in the MR sensing element that measured the variations in the magnetic field intensity caused by the air pressure variation and then turned it into an electrical signal. The MR sensing element used in this work was a highly sensitive hybrid MR sensor of planar hall–anisotropic magnetoresistive type, which uses a spin-valve film structure.

These remote tactile sensing systems showed high resolution $(300\mu N)$ and wide dynamic range (6 Pa–400 kPa) in accordance with the low noise ratio. The external vibration noise signal was only 0.17% of the maximum signal change by pressure. The output signal variation under different temperature conditions between 10°C and 80°C was approximately 2 kPa, which was much smaller compared to the cases, where the MR sensing elements were directly exposed to heat. In summary, the remote touch tips are robust to external electromagnetic and thermal noise, also interference by water without any hysteresis [22].

B. Integration Concept

The remote touch tip and the MR sensor were located separately; hence, a substantial passage was required compared to other sensors. Specifically, a tube (E = 0.5 GPa) stiffer than normal wires with an inner diameter of 1 mm and an outer diameter 2 mm was used to transfer the air pressure from the sensing tip to the magnetoresistive sensor and minimize the signal change. Implementing the substantial passage is an important issue when applying the tactile sensing system to prevent sensor interconnection breakaway from the tensile force even if the remote sensor tip moves by actuation.

In a human tactile sensing system, the nerve cells in the synapses transmit the signal inside of the body to prevent signal distortion. A rolling contact joint structure capable of having hollow channels that can easily insert the air tubes and wires was adopted to protect sensor interconnection breakaway and distortion from the external disturbance. Design optimization of the joints was required to minimize the tube length variation caused by joint rotation when the air tube passes through multiple joints.

C. Modularized Design

The modularized design concept enables easier replacement and repairs of the units, particularly the tactile sensors with a relatively high probability of wear caused by their frequent physical contact with the surroundings. A bottom-up approach of assembly also allows the structure to be rapidly built-up with a short time between iteration times. Various robot applications are pursuing modularization (e.g., customizable wearable glove and soft robots) for design and fabrication convenience [26], [27]. In this study, the sensor sensitivity and the measuring range of the modularized sensor units were changed by reassembling the elastomer membrane. The sensor and joint units were serially assembled and easily replaceable.

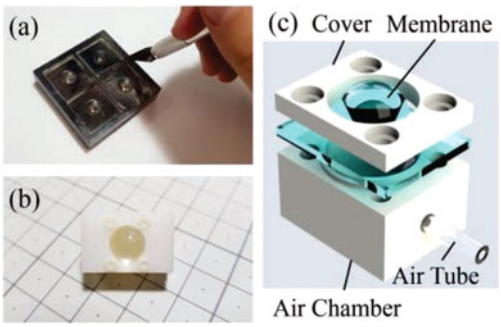

Fig. 2. Remote touch tip of the tactile sensing system: (a) elastomer membrane with the mold, (b) assembled sensor unit, and (c) schematic of the sensor unit.

III. Sensor Unit

Recent research has been investigating the characteristics of magnetic sensors used for MR sensing elements [22]. This section presents the characteristics of the developed remote sensor tip.

A. Mechanical Design

The sensor unit consisted of three components: an air chamber, an elastomer membrane for sensing, and a cover to prevent air leakage. The PDMS (Dow Corning Corp., Sylgard 184) membrane had a hemispherical sensing tip ($\phi 8\,\mathrm{mm}$) at the center on a rectangular plate. The PDMS base and a cross-linker were mixed in a 10:1 ratio, degassed using vacuum pressure, then casted on the mold. The mold was made using a 3D printer (Object260 Connex; Stratasys, Ltd.), and silver was deposited by a sputtering system for ease-of-detachment of the elastomer membrane (Fig. 2(a)).

The air chamber with a cylindrical extruded cut ($\phi 9\,\mathrm{mm} \times 6\,\mathrm{mm}$) was the main component of the sensor unit. In minimizing the air leakage, the inlet of the air chamber should have a step of 0.5 mm such that the membrane can cap the air chamber as the cover is being assembled (Fig. 2(b) and (c)). The air chamber and the cover were tightened with bolts. The air tube was tightly fitted from the side of the chamber to transmit the pressure variation. Polymeric bolts were chosen to have a sensor that can be used in water and in external electromagnetic environments.

B. Pressure Measurement Tests of the Elastomer Membrane

As the remote touch tips are being assembled, the sensor sensitivity and the sensing range were modified by replacing the elastomer membrane thickness. The modification will be useful in prosthetic hands or robotic grippers for tasks with varying pressure measurement ranges. Sensing units with a high sensitivity were required for holding fragile objects, while sensing units with a large measuring range were needed for lifting large loads.

Unit specimens with different thicknesses were fabricated to confirm the effect of the thickness change of the sensing membrane. The PDMS membranes were fabricated in three types: 0.5 mm, 0.8 mm, and 1.3 mm thicknesses. The sensor unit specimens were installed on a custom-built tactile characterization system, which can apply precise values of pressure in the steps of 25 gf and measure the output electrical voltage. Fig. 3(a) summarizes the output voltage and pressure relationships ob-

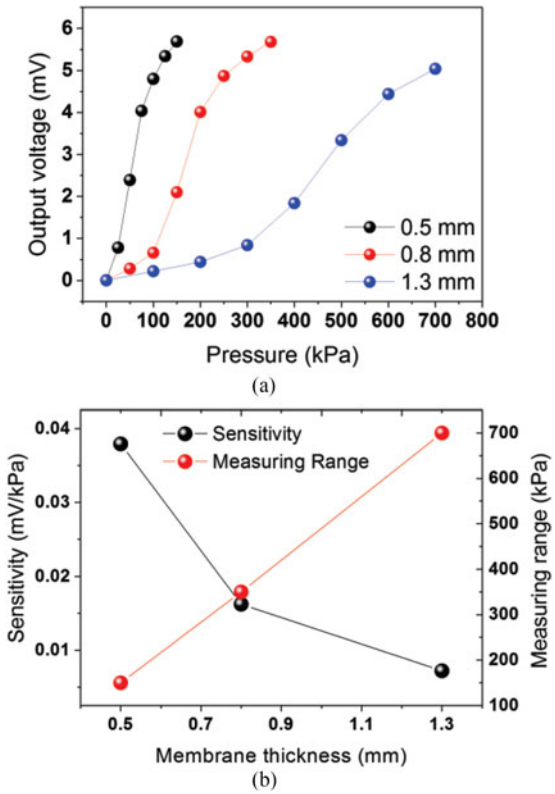

Fig. 3. Signal measurement results by membrane thickness: (a) output voltage according to the applied pressure; and (b) sensitivity (sensor output voltage/applied pressure) and measuring range (maximum measured pressure) according to the membrane thickness, showing trade-off relationships.

tained by the applied force of the system and the area of the air chamber according to the membrane thickness with no drift in voltage signal. Fig. 3(b) indicates that the sensor sensitivity increased with the decreasing membrane thickness, and was equal to 0.0072 mV/kPa at 1.3 mm, 0.016 mV/kPa at 0.8 mm, and 0.038 mV/kPa at 0.5 mm. The measuring range increased in proportion to the thickness: 150 kPa at 0.5 mm, 350 kPa at 0.8 mm, and 700 kPa at 1.3 mm.

IV. Joint Unit

Joint units were developed for the usage with a novel MR sensor with remote tactile system of the robotic hands. The design optimization of the air-transmitting tube insertion position was performed for the reliable sensor connection compared to the conventional pin joints.

A. Mechanical Design

The practical issue with embedding sensors in an application is sensor interconnection. Although the proposed tactile sensing system had a robust interconnection, the air transmission tube was still protruding outward. The air tube was inserted into the joint to prevent tube breakaway from external disturbance and overcome this problem.

The rolling contact joint unit inspired by the rolling movements of the human joints mainly comprised two circular links and straps that wrapped around the link surface [24]. The bodies constituting the joint moved relatively to each other and rotated by line contact without sliding. The center of rotation was the

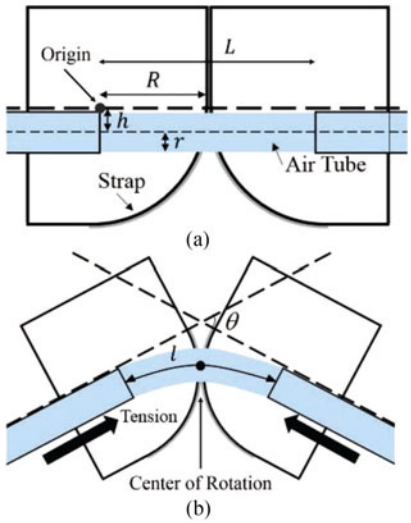

Fig. 4. Cross-sectional view of the rolling contact joint unit with embedded air tube: (a) neutral state at $\theta = 0$ and (b) bending at θ.

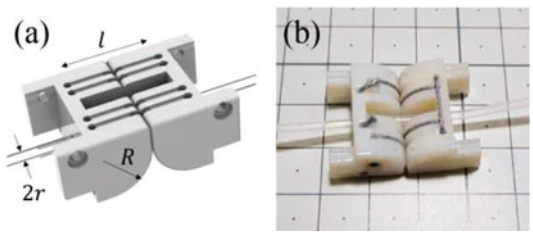

Fig. 5. Rolling contact joint unit with embedded air tube: (a) schematic view and (b) assembled joint unit.

contact point of the joint bodies; thus, the center of rotation changed when the joint rotated. As the strap connecting the links passes over the contact surfaces, the joint unit has a hollow channel in the center of the joint that enabled the tube to pass through. Although the center of the joint was hollow, the joints were strong in compression and tensile directions because of their contact characteristics. Moreover, the advantages of the rolling contact joint included avoidance of high concentrations, reduction in wear, low friction, and a large range of motion [28], [29].

Fig. 4 illustrates a schematic of the rolling contact joint unit of 7.5 mm radius (R) with the embedded air transmitting tube, where L is the initial length of the tube equal to $2R$, and $l(\theta)$ is the required length of the tube of the bending angle θ, where $l(0) = L$. An air tube of 1 mm radius (r) made by polytetrafluoroethylene penetrated the joint unit at an insertion height (h) from the center. The angle θ was limited to 0°–90° by the geometric constants of the stopper and the moment arm of the tendon (Fig. 5). The extension motion was passively produced by the restoring force of the air tube after the tendon was released.

B. Joint Unit Modeling

If the air tube is negligibly thin with no stiffness, no variation in length of the tube can be observed because the tube passes through the center of rotation of the rolling contact joint unit. However, the thickness and the bending stiffness of the air tube cannot be ignored, and the tube length changed when bending occurred in the joint (Fig. 4(b)). The tube length variation was

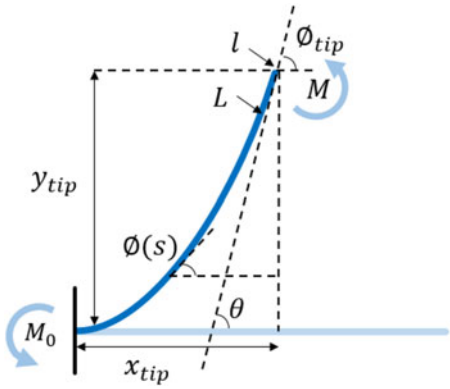

Fig. 6. Terminology used to describe the large deformation bending and the discription of the parameterized end tip.

modeled according to the bending angle to prevent tensioning of the tube that would weaken the sensor connection. We optimized the joint unit design based on the model to prevent the tensioning and minimize the length variation of the tube.

The bending angle of the tube was up to 90°; hence, a large deformation beam bending model was needed. Large deformations can be computed by numerical methods, but require more computing power and time than analytic approaches. Analytical modeling was applied to calculate the tube flexure and optimize the design. The Smooth Curvature model [30], a low-dimensional alternative to finite element models, was used to build the physical parametric models of the bending flexures constructed from the variation form of the Euler–Bernoulli equation.

$$M = EI\frac{d\phi}{ds} = EI\frac{\frac{d^2y}{dx^2}}{\left[1+\left(\frac{dy}{dx}\right)^2\right]^{\frac{3}{2}}} \tag{1}$$

$$\phi(s) = \alpha\frac{s}{L} \tag{2}$$

$$\alpha = -\frac{M_0 L}{EI} \tag{3}$$

A first-order approximation was chosen as shown in (2) because the tube was assumed to experience only pure moment loading, and the position and angle errors were correspondingly small. $\phi(s)$ is the angle of the tangent vector; α is the coefficient that describes the flexure configuration obtained by $\phi'(0)$ (3); and M_0 is the moment at the root of the flexure (Fig. 6).

$$x(s) = \int \cos(\phi(s))ds = \frac{L}{\alpha}\sin\left(\alpha\frac{s}{L}\right) \tag{4}$$

$$y(s) = \int \sin(\phi(s))ds = \frac{L}{\alpha}\left(1-\cos\left(\alpha\frac{s}{L}\right)\right) \tag{5}$$

The Cartesian profile $(x(s), y(s))$ was obtained by the integrals of the angle of the deformation $\phi(s)$ in (2).

$$\begin{pmatrix} x_{tip,r} \\ y_{tip,r} \end{pmatrix} = 2R\begin{pmatrix} \cos\frac{\theta}{2} \\ \sin\frac{\theta}{2} \end{pmatrix} + \begin{pmatrix} \cos\theta & -\sin\theta \\ \sin\theta & \cos\theta \end{pmatrix}\begin{pmatrix} 0 \\ h \end{pmatrix} - \begin{pmatrix} 0 \\ h \end{pmatrix} \tag{6}$$

$$\phi_{tip} = \theta \tag{7}$$

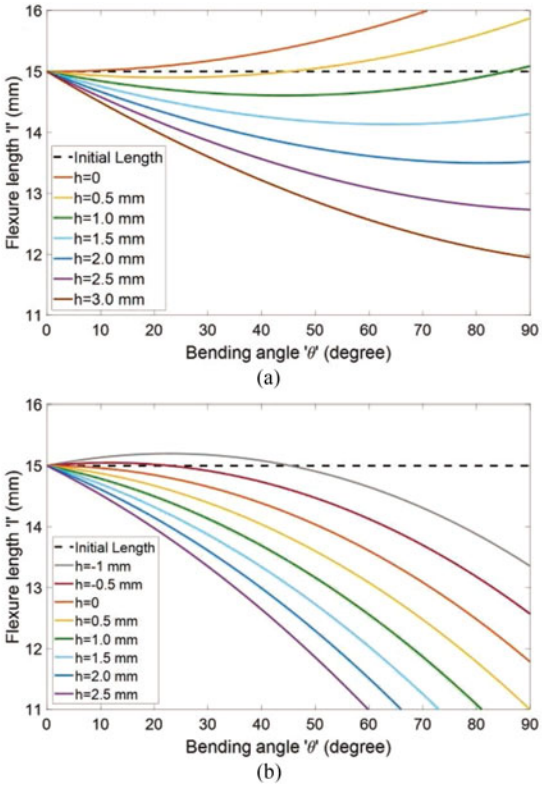

Fig. 7. Required flexure length variations according to the bending angle at the insertion height: (a) rolling contact joint and (b) pin joint.

The coordinate of the tip $(x_{tip,r}, y_{tip,r})$ of the rolling contact joint was geometrically estimated by (6), where the origin was located on the center of the joint (Fig. 4(a)). The tip angle (ϕ_{tip}) was equal to the bending angle of the joint as in (7).

$$\phi_{tip} = \theta = \phi(l) = -\frac{M_0}{EI} l \tag{8}$$

$$x_{tip} = 2\mathrm{R}\cos\frac{\theta}{2} - h\sin\theta = x(l) = \frac{L}{\alpha}\sin\left(\alpha\frac{l}{L}\right) \tag{9}$$

By obtaining (2) and (7) and (4) and (6), the required length l and M_0 are solved in nonlinear equations by (8) and (9) in terms of the bending angle.

Fig. 7(a) plots the required flexure length (l) when the bending angle (θ) changes from 0 to 90° for the rolling contact joint unit according to the insertion height (h) of the tube. The lines with different colors indicate the variation in the flexure length as the tube insertion height changes at intervals of 0.5 mm. The tube length must be 16.7 mm when the joint unit was bent to 90°, and the tube insertion height was $\mathrm{h} = 0$. In other words, the tube should be pushed into the joint by 1.7 mm.

$$\begin{pmatrix} x_{tip,p} \\ y_{tip,p} \end{pmatrix} = R\begin{pmatrix} 1+\cos\theta \\ 1+\sin\theta \end{pmatrix} + \begin{pmatrix} \cos\theta & -\sin\theta \\ \sin\theta & \cos\theta \end{pmatrix}\begin{pmatrix} 0 \\ h \end{pmatrix} - \begin{pmatrix} 0 \\ h \end{pmatrix} \tag{10}$$

The coordinate of the tip of the pin joint was estimated by (10). Fig. 7(b) indicates the flexure length corresponding to the rotating angle of the pin joint. The tube length must be 11.8 mm when the joint unit was bent to 90°, and the tube insertion height was $\mathrm{h} = 0$.

TABLE I
OPTIMIZED INSERTION HEIGHT OF THE JOINTS

	Design Parameter: Insertion height h (mm)	*Minimum length l (mm)*	*Maximum length variation $\lvert\Delta l\rvert$ (mm)*	*At angle θ*
Rolling contact joint	1.06	14.56	0.44	46.8 °
Pin joint	0	11.78	3.22	90 °

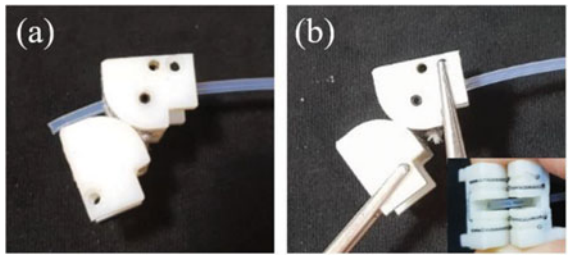

Fig. 8. Validation test of the rolling contact joint unit: (a) $\mathrm{h} = 0$ mm and (b) $\mathrm{h} = 2.06$ mm.

Two design criteria were selected to reflect the modeling into the design and prevent sensor interconnection breakaway: in the range of $0 \le \theta \le 90^\circ$, 1) the length variation $\Delta l(\theta) \le 0$ and 2) the insertion height should minimizes the $\max|\Delta l(\theta)|$. The tube was assumed unstretchable; hence, tube tensioning was more critical to the interconnection than compression, which can be compensated by beam bending. The first criterion was the constraints that needed to eliminate the tension on the air tube. The second criterion was the optimization function to minimize the compression force on the air tube. The objective parameter of the optimization was the insertion height.

Table I indicates the optimal insertion height that meets the design criteria, $\mathrm{h} = 1.06$ mm for the rolling contact joint and $\mathrm{h} = 0$ mm for the pin joints. The maximum length difference of the rolling contact joint was only 14% compared to the pin joint; thus, designing the rolling contact joint with the signal wire or the tube was advantageous for passing through.

The optimized joint unit was designed to pass the tube at 2.06 mm from the center of the circle considering the radius of the air tube (1 mm). Fig. 8 shows the difference in the joints with and without the design optimization. An un-optimized joint unit released the air tube outward when the joints bent over 90°; however, the optimized joint unit maintained the air tube in position, indicating that the tube did not push into the joint. This design methodology can be generalized to sensors that require signal transmitting wires.

V. APPLICATION

In this section, we designed a sensor array for multi-tactile sensing and assembled a three-finger gripper using sensor and joint units to integrate the sensory-motor feedback.

A. Sensor Array

The MR sensing element was fabricated using DC magnetron sputtering and a lift-off process. According to Fig. 9, magnetic

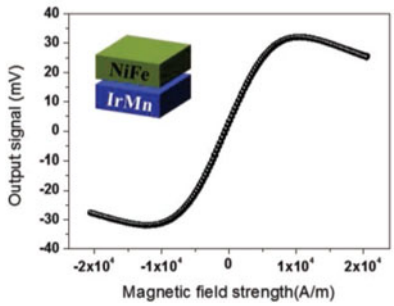

Fig. 9. Output signal profile of MR Sensor: the MR sensor element consists Ta/Ni/Fe/IrMn/Ta thin film with a bilayer structure.

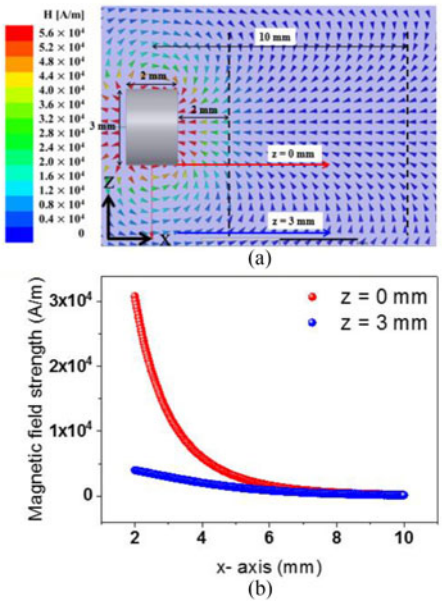

Fig. 10. Finite element simulation to set the position of permanent magnets. (a) Simulated magnetic field that proceeds using a cylindrical permanent magnet. The vector color visualizes the magnetic field strength and the exact directions of the magnetic field on the MR sensor. The field directions are changed based on the relative vertical and horizontal positions of the MR sensor to the permanent magnet. (b) Each profile of the magnetic field changes the intensity of the magnetic field from 2 mm to 10 mm. The intensity of the magnetic field is almost zero after 10 mm.

multilayers (bilayer structure) of Ta (5 nm)/ NiFe (10 nm)/IrMn (10 nm)/Ta (5 nm) were deposited by a DC magnetron sputtering system (magnetic field sensitivity: 31 mV/A·m^{-1}).

A finite element simulation (ANSYS, Maxwell 16.1) was performed to analyze the initial position of a cylindrical permanent magnet ($\phi 3\,\mathrm{mm} \times 2\,\mathrm{mm}$) with the MR sensor array (Fig. 10). The change in the intensity of the magnetic field in the linearly varying section of the MR sensor was from 2 mm to 10 mm (x axis).

The permanent magnet was embedded in the elastomer membrane (Ecoflex 0030) and moved toward the MR sensing element as air pressure was applied to the membrane. The initial vertical and horizontal distances of the permanent magnet for the MR sensor were optimized to be 3 mm and 2 mm, respectively, through the magnetic field sensitivity of MR sensor and Maxwell simulation. The minimum distance that the other sensors were not affected by the magnetic field was 10 mm

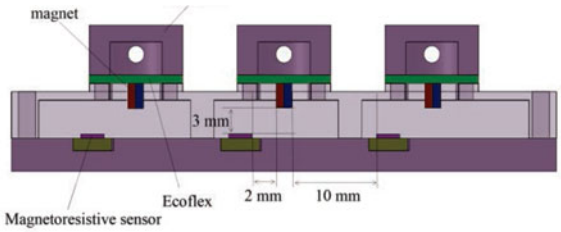

Fig. 11. Schematic of the MR sensing element placement of the sensor array system.

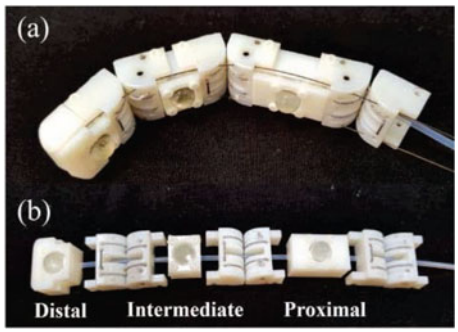

Fig. 12. Assembled units that forms a robotic finger: (a) robotic finger with the remote touch tips, and (b) tubing with the distal phalanx.

(Fig. 11). Through the simulation, a sensor array system with three MR sensing elements was fabricated and used to acquire the grasping experimental data.

B. Module Assembly

A tendon-driven finger was constituted by alternately assembling the sensor and joint units. As shown in Fig. 12(a), fabricate sensor units of the desired length first, then connect the air tube to the sensor unit that penetrates through the other joint and sensor units. After bolting the sensor and joint units, route the tendon that passes sideways of the sensing units to not interrupt with tactile sensing. Lastly, air tubes were connected to the MR sensor array system. In this way, multiple units can be used to form various combinations of drivable and sensible structures.

We implemented a remote sensing tip per finger in this application. However, by taking advantage of the sensor unit being replaceable, we easily changed the position of the units by replacing the tube and the remote sensor unit. In Fig. 12(b), an air tube was connected to the sensor unit in the distal phalanx by replacing the sensor unit and rearrange the air tube.

C. Three-Finger Gripper Design

A tendon-driven three-finger gripper was assembled to develop the medium wrap, which was most frequently used for the longest duration of daily life [31]. The gripper had three fingers corresponding to the index, middle, and thumb that faced each other to hold a cylindrical shaped object. Each finger was designed to have an anthropomorphic characteristic. Each finger consisted of three segments with a ratio of human fingers: distal, intermediate, and proximal phalange. The index and middle fingers were actuated by the tendons functioning as a flexor with an underactuated mechanism using a differential mechanism into one actuator. Specifically, a tendon passes through the in-

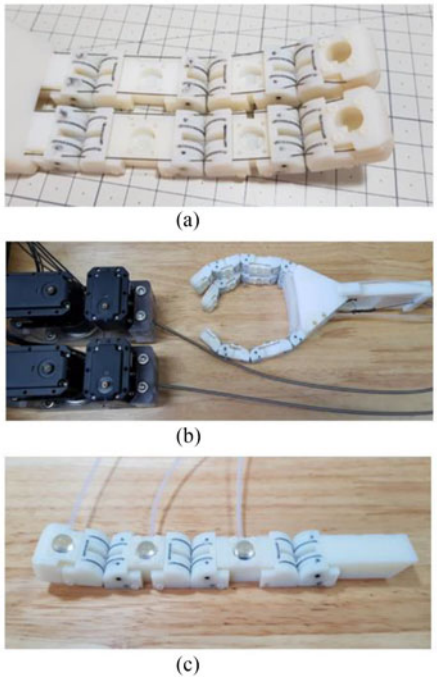

Fig. 13. Overview of the assembled three-finger gripper: (a) differential mechanism by an underactuated tendon routing path, (b) three-finger gripper system with slack enabling actuators, and (c) reference setup of the tactile sensor placement: thumb.

dex and middle fingers in parallel (Fig. 13(a)). This differential mechanism helped achieve adaptation of different objects using actuators fewer than the number of fingers [32]. The thumb was flexed by another actuator such that the gripper had a total of two actuating degrees of freedom. For tendon-driven actuating, slack enabling actuators were adapted to prevent the spool derailment (Dynamixel MX-106, MX-28, ROBOTIS) [33]. Elastic kink-free tendons transmitted force to the gripper through the spring sheaths (Fig. 13(b)).

This section considers the problem of positioning the sensor to simplify the tubing, equalize the stiffness of each joint, and obtain the most useful data showing maximal signals by grasping cylinders of various sizes. The candidate position that the tactile sensors were to be embedded into was each phalanx (distal, intermediate, and proximal) of the finger.

For this purpose, a finger reference setup embedded with a tactile sensor in each phalanx was assembled to verify the most sensitive position among the phalanges (Fig. 13(c)). In this setup, the air tubes were located on the side of the sensor unit that did not penetrate the joint unit. Additional air tubes were located in the joint units for the reference setup such that the joint units had a similar joint stiffness. For high sensitivity, 0.5 mm-thickness elastomer membranes were adopted inside the remote touch tips. The output voltage variations of each tactile sensor were measured when a cylinder of 50, 60, 70, and 80 mm in diameter was gripped with the reference setup. The voltage variations were measured when the tendon was pulled by one step stroke (0.46 mm).

The tactile sensor located in the intermediate phalanx did not show any signal change about all the objects because no contact occurred (Fig. 14). Except for grasping the largest cylinder with 80 mm diameter, the tactile sensor on the distal phalanx was able to measure the highest and constant output voltage signal by making contact in all sensed cylinders. The goal of the three-

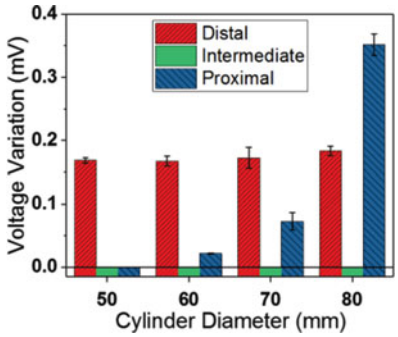

Fig. 14. Experimental results of the output voltage variations according to the cylinder diameter measured by the reference setup finger. Error bars represent the standard deviation and bars represent the mean values.

Fig. 15. Experimental setup for measuring sensing data with the tactile sensor array system. Red signal: index finger, white signal: middle finger, green signal: thumb.

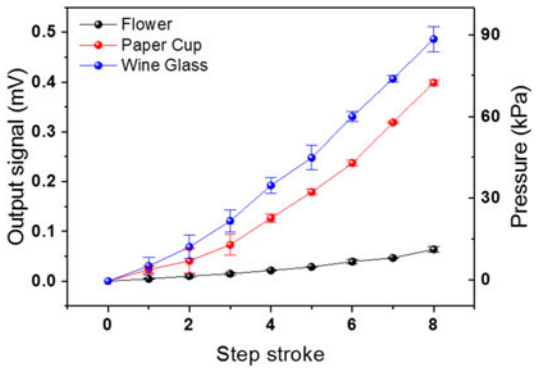

Fig. 16. Experimental results of the output voltage signals when wrapping the objects with various compliance: flower, paper cup, and wine glass. Error bars represent the standard deviation and bars represent the mean values.

finger gripper was to grasp various sizes of cylindrical objects; thus, the remote touch tips were attached to each distal phalanx to sense diverse objects with high sensitivity.

D. Grasping Objects With Various Compliance

Objects with different compliance and that were easily deformable or fragile were selected because they were commonly manipulated in daily life. They were used to confirm the performance of the robotic hand with tactile sensors. Three trials of each evaluation experiment were conducted to measure the pressure by gripping flowers, paper cups, and wine glasses to verify the assembled three-finger gripper. Subsequently, a 0.8 mm membrane was adopted in the sensor tip to achieve both sensitivity and measuring range to grasp objects with various

compliance. The output voltage thresholds were individually set by the preliminary tests to accomplish the sensory feedback, that is, enough pressure to lift the objects, but not to eject the objects because of the high tension of the tendon. A feedback loop with amplified output signals was constructed to hold the object until the tactile signals exceeded the threshold voltage when the robotic fingers were flexed by the tendon of the step stroke (Fig. 15) (Controller: OpenCM9.04 with 485 expansion board, ROBOTIS). According to Fig. 16, the radial direction compliance of each object was compared with the increasing signals with the stroke. The wine glass and the paper cup showed 7.6 and 6.2 times higher values than the flower.

VI. Conclusion

This study presented sensor and joint units for the assembly of tactile embedded robotic hands. We adopted the rolling contact joint design for ease-embedding the signal wires or tubes inside and proved that the rolling contact joints were suitable in preventing tube tensioning. This phenomenon occurred because the center of rotation of the rolling contact joint followed the flexure trajectory of the internal tube when the joint rotated, minimizing the length variation. Thanks to the MR tactile sensor system with the remote touch tip, creating applications that are less affected by the surrounding environment is possible. In the meantime, the sensitivity and the measuring range of the sensors could be altered by exchanging the elastomer membrane thickness.

The unit module could be assembled and reassembled to enable the prototyping of robots that end users can use to quickly and easily obtain tactile data. Moreover, for the future work, the assembled robotic applications are expected to be used in extreme environments rather than only in ordinary or less extreme environments. For instance, autonomous robotic hands that help the activities of daily living should be able to function and sense even in situations, such as dishwashing, which are activities that need to be in contact with water (multimedia materials). Magnetic resonance imaging (MRI)-compatible grippers for external electrical and magnetic conditions are expected to be used by integrating the remote tactile system.

Acknowledgment

The authors would like to thank J. J. Song for working on the figures.

References

[1] R. S. Dahiya, G. Metta, M. Valle, and G. Sandini, "Tactile sensing — From humans to humanoids," *IEEE Trans. Robot.*, vol. 26, no 1, pp. 1–20, Feb. 2010.

[2] N. Yogeswaran *et al.*, "New materials and advances in making electronic skin for interactive robots," *Adv. Robot.*, vol. 29, pp. 1359–1373, 2015.

[3] A. M. Almassri *et al.*, "Pressure sensor: State of the art, design, and application for robotic hand," *J. Sensors*, vol. 2015, 2015, Art. no. 846487.

[4] R. S. Dahiya, P. Mittendorfer, M. Valle, G. Cheng, and V. J. Lumelsky, "Directions toward effective utilization of tactile skin: A review," *IEEE Sensors J.*, vol. 13, no. 11, pp. 4121–4138, Nov. 2013.

[5] P. Mandlik, S. P. Lacour, J. W. Li, S. Y. Chou, and S. Wagner, "Fully elastic interconnects on nanopatterned elastomeric substrates," *IEEE Electron Device Lett.*, vol. 27, no. 8, pp. 650–652, Aug. 2006.

[6] Y.-L. Park, B.-R. Chen, and R. J. Wood, "Design and fabrication of soft artificial skin using embedded microchannels and liquid conductors," *IEEE Sensors J.*, vol. 12, no. 8, pp. 2711–2718, Aug. 2012.

[7] M. Amjadi, A. Pichitpajongkit, S. Lee, S. Ryu, and I. Park, "Highly stretchable and sensitive strain sensor based on silver nanowire–elastomer nanocomposite," *ACS Nano*, vol. 8, pp. 5154–5163, 2014.

[8] S. Lee *et al.*, "A transparent bending-insensitive pressure sensor," *Nature Nanotechnol.*, vol. 11, pp. 472–478, 2016.

[9] W. Dang, V. Vinciguerra, L. Lorenzelli, and R. Dahiya, "Printable stretchable interconnects," *Flexible Print. Electron.*, vol. 2, 2017, Art. no. 013003.

[10] H. Shinoda and H. Oasa, "Wireless tactile sensing element using stress-sensitive resonator," *IEEE/ASME Trans. Mechatronics*, vol. 5, no. 3, pp. 258–265, Sep. 2000.

[11] K. Yamada, Y. Nakajima, N. Koshida, K. Goto, and H. Shinoda, "Wire-free tactile sensing element based on optical connection," in *Proc. Tech. Dig. Sensor Symp.*, 2002, pp. 433–436.

[12] M. I. Tiwana, S. J. Redmond, and N. H. Lovell, "A review of tactile sensing technologies with applications in biomedical engineering," *Sens. Actuators A, Phys.*, vol. 179, pp. 17–31, 2012.

[13] M. H. Lee, "Tactile sensing: New directions, new challenges," *Int. J. Robot. Res.*, vol. 19, pp. 636–643, 2000.

[14] C. G. Núñez, W. T. Navaraj, E. O. Polat, and R. Dahiya, "Energy — Autonomous, flexible, and transparent tactile skin," *Adv. Funct. Mater.*, vol. 27, 2017, Art. no. 1606287.

[15] J. Kim *et al.*, "Stretchable silicon nanoribbon electronics for skin prosthesis," *Nature Commun.*, vol. 5, 2014, Art. no. 5747.

[16] Y. Tenzer, L. P. Jentoft, and R. D. Howe, "The Feel of MEMS Barometers: Inexpensive and easily customized tactile array sensors using MEMS barometers chips," *IEEE Robot. Autom. Mag.*, vol. 21, no. 3, pp. 89–95, Sep. 2014.

[17] D. Goger, N. Gorges, and H. Worn, "Tactile sensing for an anthropomorphic robotic hand: Hardware and signal processing," in *Proc. IEEE Int. Conf. Robot. Autom.*, 2009, pp. 895–901.

[18] A. Akhtar *et al.*, "A low-cost, open-source, compliant hand for enabling sensorimotor control for people with transradial amputations," in *Proc. 38th Annu. Int. Conf. IEEE Eng. Med. Biol. Soc.*, 2016, pp. 4642–4645.

[19] Z. Su *et al.*, "Force estimation and slip detection for grip control using a biomimetic tactile sensor," in *Proc. IEEE-RAS 15th Int. Conf. Hum. Robots*, 2015, pp. 297–303.

[20] A. Cloutier and J. Yang, "Design, control, and sensory feedback of externally powered hand prostheses: A literature review," *Crit. Rev. Biomed. Eng.*, vol. 41, pp. 161–181, 2013.

[21] M. Kaboli, R. Walker, and G. Cheng, "In-hand object recognition via texture properties with robotic hands, artificial skin, and novel tactile descriptors," in *Proc. IEEE-RAS 15th Int. Conf. Hum. Robots*, 2015, pp. 1155–1160.

[22] S. Oh *et al.*, "Remote tactile sensing system integrated with magnetic synapse," *Sci. Rep.*, vol. 7, 2017, Art. no. 16963.

[23] B. M. Hillberry and A. S. Hall, Jr., "Rolling contact joint," U.S. Patent US3932045A, Jan. 13, 1976.

[24] P. A. Halverson, "Multi-stable compliant rolling-contact elements," M.S. thesis, Dept. Mech. Eng., Brigham Young Univ., Provo, UT, USA, 2007.

[25] L. Jogschies *et al.*, "Recent developments of magnetoresistive sensors for industrial applications," *Sensors*, vol. 15, pp. 28665–28689, 2015.

[26] S.-S. Yun, B. B. Kang, and K.-J. Cho, "Exo-glove PM: An easily customizable modularized pneumatic assistive glove," *IEEE Robot. Autom. Lett.*, vol. 2, no. 3, pp. 1725–1732, Jul. 2017.

[27] J.-Y. Lee, W.-B. Kim, W.-Y. Choi, and K.-J. Cho, "Soft robotic blocks: Introducing SoBL, a fast-build modularized design block," *IEEE Robot. Autom. Mag.*, vol. 23, no. 3, pp. 30–41, Sep. 2016.

[28] S.-H. Kim, H. In, J.-R. Song, and K.-J. Cho, "Force characteristics of rolling contact joint for compact structure," in *Proc. 6th IEEE Int. Conf. Biomed. Robot. Biomechatronics*, 2016, pp. 1207–1212.

[29] M. G. Catalano, G. Grioli, E. Farnioli, A. Serio, C. Piazza, and A. Bicchi, "Adaptive synergies for the design and control of the Pisa/IIT SoftHand," *Int. J. Robot. Res.*, vol. 33, no. 5, pp. 768–782, 2014.

[30] L. U. Odhner and A. M. Dollar, "The smooth curvature model: An efficient representation of Euler–Bernoulli flexures as robot joints," *IEEE Trans. Robot.*, vol. 28, no. 4, pp. 761–772, Aug. 2012.

[31] T. Feix, J. Romero, H.-B. Schmiedmayer, A. M. Dollar, and D. Kragic, "The GRASP taxonomy of human grasp types," *IEEE Trans. Human–Mach. Syst.*, vol. 46, no. 1, pp. 66–77, Feb. 2016.

[32] H. In, B. B. Kang, M. Sin, and K.-J. Cho, "Exo-glove: A wearable robot for the hand with a soft tendon routing system," *IEEE Robot. Autom. Mag.*, vol. 22, no. 1, pp. 97–105, Mar. 2015.

[33] H. In, U. Jeong, H. Lee, and K.-J. Cho, "A novel slack-enabling tendon drive that improves efficiency, size, and safety in soft wearable robots," *IEEE/ASME Trans. Mechatronics*, vol. 22, no. 1, pp. 59–70, Feb. 2017.